Convection Measurement Apparatus and Methodology

Aubrey G. Jaffer
agj@alum.mit.edu

Abstract

Presented are the design and operating methodology of an apparatus constructed to make measurements of forced convection from an isothermal plate with a precisely rough surface. Measurements with a 2.4% root-sum-squared measurement uncertainty were achieved.

Mixed convection measurements at various plate orientations were also made, driving the development of a theory of turbulent mixed convection from any rectangular plate having at least one horizontal edge.

Keywords: mixed convection; forced convection; wind-tunnel

Table of Contents

1. Introduction

Starting in 2015 an apparatus was constructed to measure forced convection in air from a heated 305 mm square plate with precisely 3 mm of roughness. Although optimized for downward natural convection mixed with horizontal forced flow, because of the small size of the wind-tunnel chassis (1.3 m × .65 m × .65 m), it also afforded an opportunity to characterize mixed convection at various orientations of plate and flow.

While the total convection could be derived from local convection, measurements of local convection necessarily can't provide complete coverage of a test surface (particularly the leading edge). Instead, the apparatus was designed to measure total heat flow (and total convection). This decision was fortuitous in that forced convection measurements with ±2.4% root-sum-squared (RSS) measurement uncertainty were achieved.

The operating methodology was unusual in that it didn't wait for temperatures to stabilize before taking measurements. Instead it captured a time sequence of all measured quantities and inferred the convection from that dynamic sequence.

The measurements obtained were the basis for two papers: *Skin-Friction and Forced Convection from Rough and Smooth Plates* [1] and *Mixed Convection From an Isothermal Rough Plate* [2].

The Section 12 appendix builds a convection formula for the bi-level plate which models the transition from rough turbulent convection to smooth turbulent convection at increasing Reynolds numbers.

2. Apparatus

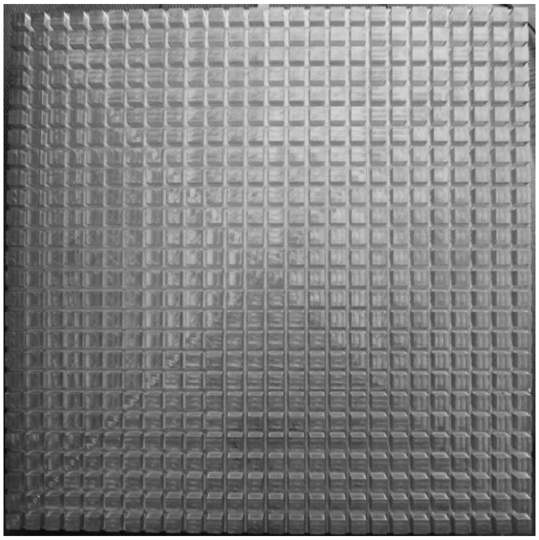

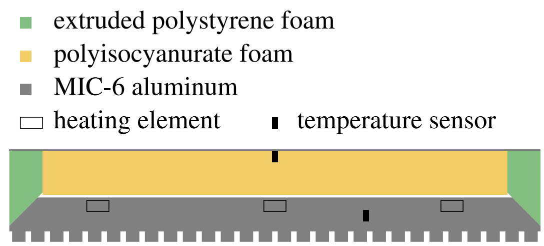

Figure 1 rough surface of plate **Figure 2 cross-section of plate assembly**

The goal was to measure forced convection from a rough plate over the widest practical span of Re.

Figure 1 shows the rough surface of the test plate; it was milled from a slab of MIC-6 aluminum to have (676 of) square $8.5\,\text{mm} \times 8.5\,\text{mm} \times 6\,\text{mm}$ posts spaced on 11.7 mm centers over the 30.5 cm $\times$ 30.5 cm plate. The area of the top of each post was $0.722\,\text{cm}^2$, which was 53% of its $1.37\,\text{cm}^2$ cell. The RMS height-of-roughness $\varepsilon = 3.00$ mm. Openness $\Omega \approx 47\%$. Embedded in the plate are 9 electronic resistors as heating elements and an LM35 temperature sensor. 2.54 cm of thermal insulating foam separates the back of the plate from a 0.32 mm thick sheet of aluminum with an LM35 temperature sensor at its center. Figure 2 is a cross-section illustration of the plate assembly.

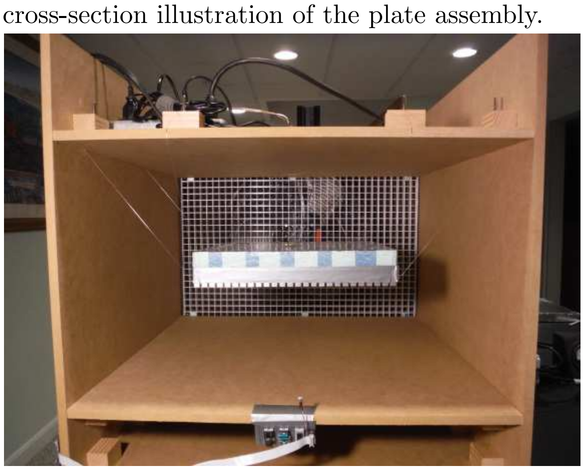

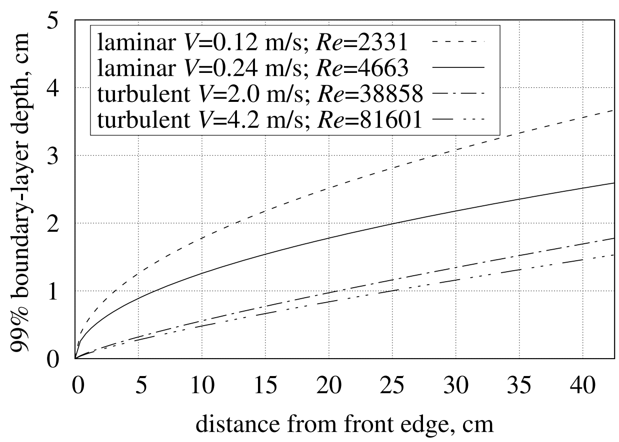

Figure 3 $\varepsilon = 3$ mm **plate in wind-tunnel** **Figure 4 wind-tunnel boundary-layers**

In order to guarantee isobaric flow, the wind-tunnel must be large enough that the boundary-layers of the test chamber and plate assembly do not interact.

The wind-tunnel test chamber in Figure 3 has a 61 cm $\times$ 35.6 cm cross-section and a 61 cm depth. This allows the plate assembly to be centered in the wind-tunnel with 15 cm of space on all sides. The fan pulling air through the test chamber produces a maximum airspeed of 4.25 m/s ($Re \approx 9 \times 10^4$ along the 30.5 cm square plate). Its minimum nonzero airspeed is 0.12 m/s ($Re \approx 2300$).

The wind-tunnel laminar and smooth turbulent 99% boundary-layer thicknesses (Schlichting [3]) are:

$$\delta_\lambda = 4.92 \sqrt{\frac{x\nu}{u}} \qquad \delta_\sigma = 0.37\, x^{4/5} \left(\frac{\nu}{u}\right)^{1/5} \tag{1}$$

Figure 4 shows that the 15 cm clearance between the plate and the test chamber walls is sufficient to prevent their boundary-layers from interacting at airspeeds within the fan's capabilities.

Rotations of the fan impeller are sensed by a fan blade interrupting an infrared beam. A microprocessor controls a solid-state relay (supplying power to the fan) to maintain a fan rotation rate, ω, which is dialed into switches. At $\omega \le 500$ r/min, the microprocessor pulses power to the fan to phase-lock the beam interruption signal to an internal clock. At $\omega > 500$ r/min, the microprocessor servos the duty cycle of a 10 Hz square-wave which gates power to the fan. This system operates at 32 r/min $< \omega <$ 1500 r/min.

The correspondence between fan rotation rate ω and empty test chamber airspeed u was determined using an "ABM-200 Airflow & Environmental Meter"; it specifies an accuracy of $\pm 0.5\%$ of reading between 2.2 m/s and 62.5 m/s. An "Ambient Weather WM-2" anemometer measured u with the rebuilt cowling.

Faster fan rotation rates yield diminishing increases of airspeed, suggesting formula (2), where u_u is the flow for arbitrarily fast rotation. With the lower inset parameter values, Figure 5 shows the measurements, fit, and RMSRE statistics at 800 r/min $\le \omega \le$ 1550 r/min for the original and rebuilt cowling.

$$u(\omega) = \left[\left[\frac{\omega}{\omega_r} \right]^{-2} \left[u_r^{-2} - u_u^{-2} \right] + u_u^{-2} \right]^{-1/2} \tag{2}$$

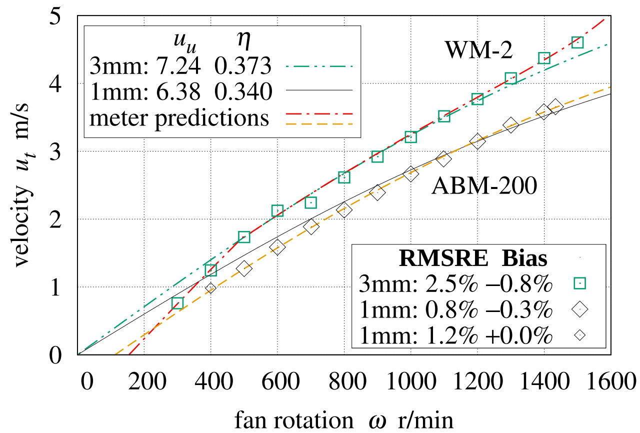

Figure 5 airspeed vs fan rotation

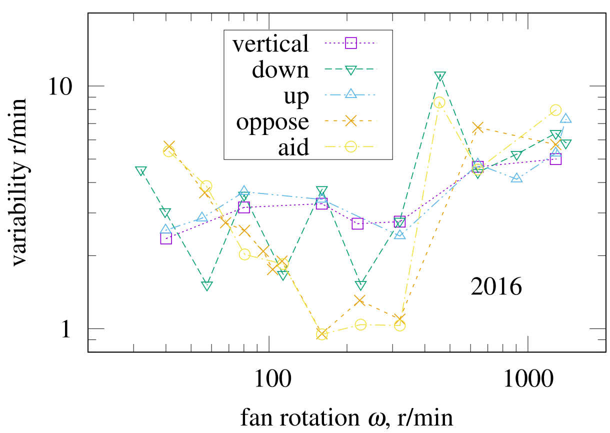

Figure 6 fan PLL variability 3 mm

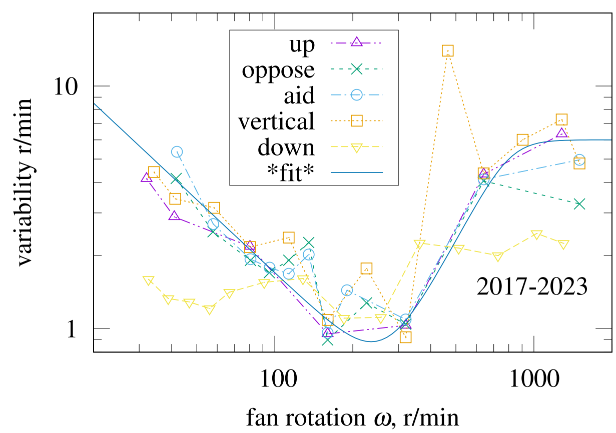

Figure 7 fan PLL variability 1 mm

Figures 6 and 7 show the fan speed variability for the experiments in each orthogonal orientation. The variability is an input to the computation of expected measurement uncertainty in Section 9. The difference between the two figures reflects refinements of the fan-control firmware.

The plate assembly is suspended from six lengths of 0.38 mm-diameter steel piano wire, which are terminated at twelve zither tuning pins in wooden blocks fastened to the outside of the test chamber. The wire is sheathed by 0.95 mm Teflon tubing where it would otherwise contact the plate metal.

The plate is suspended face down to minimize the natural convection from the test surface.

With the plate assembly in the test chamber, the airspeed increases in proportion to the reduction of test chamber aperture A_e by the plate's cross-sectional area $A_\times$:

$$\frac{u'}{u} = \frac{A_e}{A_e - A_\times} \approx 107.7\% \tag{3}$$

A four-wire suspension was used before the six-wire suspension was installed on 2016-09-11. The early upward-facing measurements flipped the plate in the four-wire suspension, whose adjustment range did not quite reach center of the test chamber; the clearance above the plate was then less than the clearance below, and the flow speed on the rough top side of the plate assembly increased. This affected the $Re > 10^4$ measurements, which should have been little affected by orientation. Scaling Re by +4% brings the measured convection into agreement with the downward and subsequent centered measurements using the six-wire suspension.

On 2017-05-29, the wind-tunnel cowling was opened in order to repair a broken wire to the plate heater. Not realized at the time, the reassembled cowling had a leak. The apparatus was moved to Waltham several months later. Trying to re-calibrate the fan-rpm-to-airspeed curve, the leak was discovered; once repaired, the calibration curve matched the previous one.

Eventually, all the 1 mm roughness measurements will be redone with an intact cowling. The existing data can be partially salvaged, however, by scaling Re by +7%. For those data sets, the expected measurement bias for airspeed is also increased 7%.

Data capture and control of convection experiments are performed by an "STM32F3 Discovery 32-Bit ARM M4 72MHz" development board. The program written for the STM32F3 captures readings and writes them to the microprocessor's non-volatile RAM, controls the plate heating, servos the fan speed, and (later) uploads the captured data to a laptop computer over a USB cable. Once per second during an experiment, the program calibrates and reads each on-chip 12 bit analog-to-digital converter 16 times, summing the sixteen 12 bit readings to create a 16 bit reading per converter.

Figure 8 shows the ambient sensor board which is at the lower edge of the tunnel in Figure 3. It measures the pressure, humidity, and temperature of the air at the wind-tunnel intake. The LM35 temperature sensor projects into the tunnel; it is wrapped in aluminum tape to minimize radiative heat transfer. To minimize self-heating, it is necessary to power the LM35 only while it is being sampled.

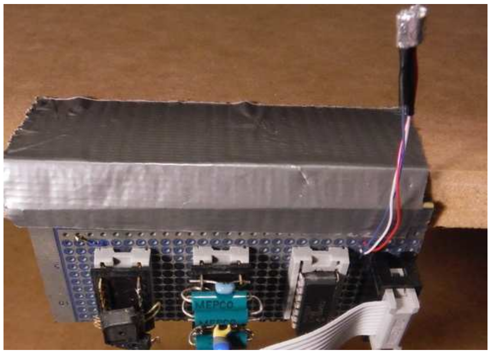

Figure 8 ambient sensors

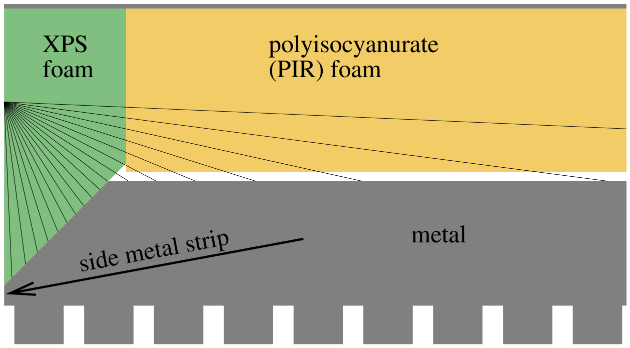

Figure 9 XPS wedge conduction

3. Measurement methodology

The measurement methodology employed is unusual. Instead of waiting for the plate to reach thermal equilibrium, the plate is heated to 15 K above ambient, the fan is started, and the sensor readings are captured every second of 102 minutes as convection cools the plate.

The physical parameters from measurements and material specifications of both plate versions are:

Table 1 physical parameters

ε_q	2.997 mm	1.129 mm	RMS height-of-roughness
A_p	0.093 m^2	0.093 m^2	plate test area
D_{Al}	0.0194 m^2	0.0194 m^2	metal slab thickness
C	4690 J/K	4242 J/K	plate thermal capacity
C_{bk}	146 J/K	146 J/K	back thermal capacity
U_I	0.075 W/K	0.075 W/K	insulation thermal conductance
ϵ_p	0.04	0.04	plate surface emissivity
ϵ_{wt}	0.90	0.90	wind-tunnel test chamber emissivity

The effective wind-tunnel emissivity ϵ_{wt} may differ from the emissivity of medium-density-fiberboard (0.90 [4]) because the temperatures of the (internal) wind-tunnel surfaces may not be uniform; the plate also exchanges thermal radiation with objects in the room which may have different emissivities and temperatures than the wind-tunnel and air.

MIC-6 aluminum was chosen for its low emissivity ($\epsilon_p = 0.04$); the radiative heat loss from the rough face of the plate is only 20 mW/K, which is about 2% of the 1.08 W/K expected for $u = 1$m/s convection.

The measured dynamic physical quantities are:

Table 2 dynamic quantities

Π_H	W	heater power
u	m/s	fluid velocity (from fan rotation rate)
T_P	K	plate temperature
T_F	K	fluid (air) temperature
T_B	K	back surface temperature

At low flow rates, the sides can leak more heat than the rough surface. The side heat transfers are simulated in order to discount them from the total heat flow. The calculated and simulated quantities are:

Table 3 calculated and simulated quantities

$U_S(u)$	W/K	side thermal conductance
h_R	W/(m^2K)	radiative surface conductance
$h(u,t)$	W/(m^2K)	convective surface conductance
$U_P(u,t)$	W/K	convective thermal conductance
$T_P(u,t)$	K	plate surface temperature
$U_{B0}(t)$	W/K	back natural convective conductance
$T_B(u,t)$	K	back surface temperature

$U_S(u)$ from equation (16) in Section 8 is the amount of radiative emissions and natural convection from the sides which reduces the convection from the test surface.

U_{B0} from equation (13) in Section 8 is the amount of natural convection from a downward-facing back face which reduces the convection from the upward-facing test surface.

4. **Heat balance**

Collecting terms which have a factor of $\overline{T_P} - \overline{T_F}$ into $U_T(u)$, the heat balance equation for the plate in mixed convection is:

$$
\begin{aligned}
U_T(u) &= U_S(u) + h(u)\,A_p + \epsilon_p\,\epsilon_{wt}\,h_R\,A_p \\
\Pi_H &= U_T(u)\,\left[\overline{T_P} - \overline{T_F}\right] + U_I\left[\overline{T_P} - \overline{T_B}\right] + U_{B0}\,\left[\overline{T_B} - \overline{T_F}\right] + C\,\frac{\mathrm{d}\overline{T_P}}{\mathrm{d}t}
\end{aligned} \tag{4}
$$

To track temperature measurements as functions of time requires characterization of the temperature-time responses of the thermal masses and insulation (assembled from pieces of polyisocyanurate (PIR) and XPS foams). Figure 10 shows the temperature-time response of the downward-facing plate to a 57.5 W step in heat drive applied starting at second 151. The dashed line is the temperature expected with a 15 s delay. Figure 10 and the heating phase of experiments show that a 15 s delay models the system well.

The temperature-time response of the insulation is best ascertained with the plate facing up so that the back is facing down for its minimum convection. Not a step response, this is the response to the plate's temperature ramp. The blue trace showing back temperature in Figure 11 is superimposed on a red trace which models the insulation as thermal conductance $U_I = 75$ mW/K with a 110 s delay between the plate and the back.

Including the delays for the insulation and plate thermal masses, and isolating $\overline{T_P}(t)$:

$$
\overline{T_P}(t) = \frac{\Pi_H(t-14) + U_T(u)\,\overline{T_F}(t) + U_I\,\overline{T_B}(t-110) - U_{B0}\,\left[\overline{T_B}(t) - \overline{T_F}(t)\right] - C\,\mathrm{d}\overline{T_P}(t)/\mathrm{d}t}{U_T(u) + U_I} \tag{5}
$$

Forced convection measurements are usually presented as $\overline{Nu}$ versus Re. In order to obtain $\overline{Nu} = h\,L/k$, equation (5) is solved for $U_P = h(u)\,A_p$, where $h(u)$ is from expanding $U_T(u)$ from equation (4):

$$
\begin{aligned}
\eta(u,t) &= \Pi_H(t-14) - U_I\,\left[\overline{T_P}(t) - \overline{T_B}(t-110)\right] - U_{B0}\,\left[\overline{T_B}(t) - \overline{T_F}(t)\right] \\
U_P(t) &= \frac{\eta(u,t) - C\,\left[\overline{T_P}(t) - \overline{T_P}(t')\right]/[t-t']}{\overline{T_P}(t) - \overline{T_F}(t)} - A_p\,\epsilon_p\,\epsilon_{wt}\,h_R - U_S(u)
\end{aligned} \tag{6}
$$

In the denominator of equation (6), $\overline{T_P}(t)$ and $\overline{T_F}(t)$ are the 11-element cosine averages of plate and fluid temperature (centered at time t). Averaging is needed so that the derivative doesn't correlate with the denominator, causing bias.

In order to simulate T_P from the other dynamic inputs, solve (5) as a finite-difference equation where $\mathrm{d}t = t - t'$:

$$
\begin{aligned}
H(u,t) &= \Pi_H(t-14) + U_T(u)\,\overline{T_F}(t) + U_I\,\overline{T_B}(t-110) - U_{B0}\,\left[\overline{T_B}(t) - \overline{T_F}(t)\right] \\
T_P(t) &= \frac{H(u,t)\,[t-t'] + C\,T_P(t')}{[U_T(u) + U_I]\,[t-t'] + C}
\end{aligned} \tag{7}
$$

In equation (7), $T_P(t')$ is the previous simulated value (not the measured value).

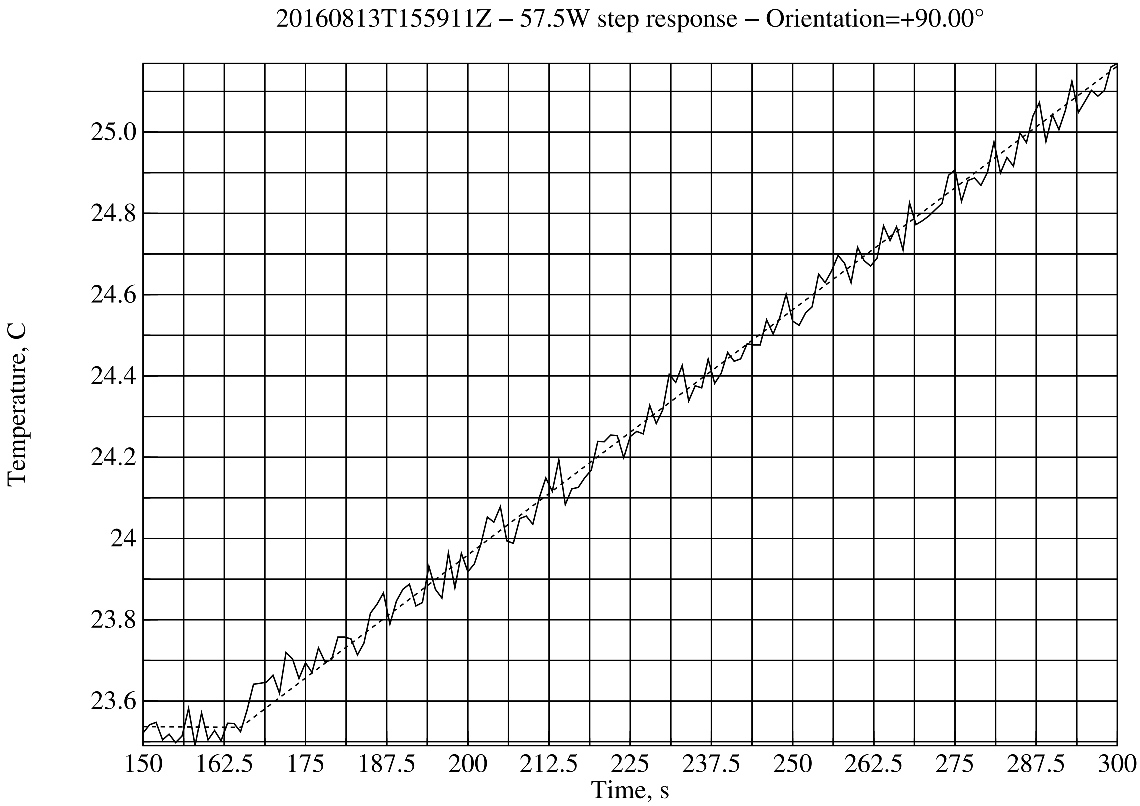

Figure 10 57.5 W step response

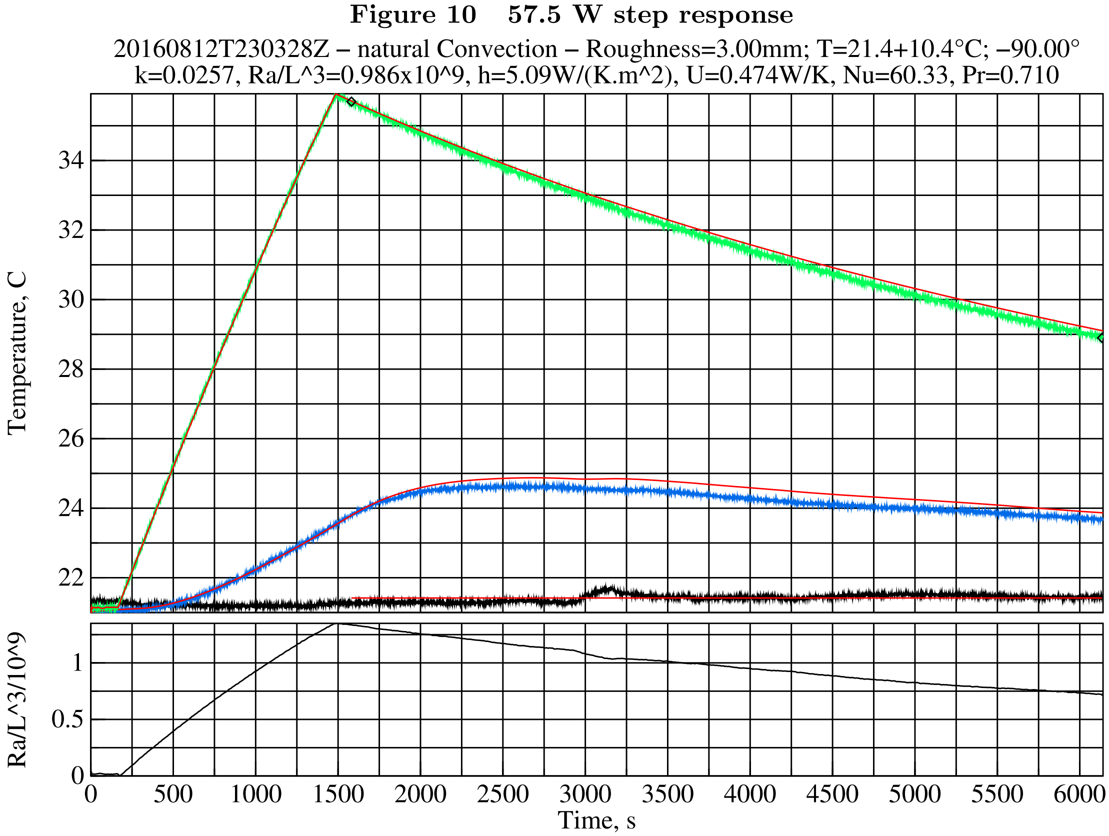

Figure 11 upward-facing natural convection run

5. **Partially obstructed natural convection**

Jaffer [5] gives a general Formula (9) for natural convection from a plate in terms of seven parameters:

- L is characteristic length; note that $Ra \propto L^3$.
- Nu_0 is static conduction.
- E is the count of 90° changes in direction of fluid flow.
- B is the sum of the mean lengths of flows parallel to the plate divided by L.
- C is the plate area fraction responsible for flow induced heat transfer.
- D is the effective length of heat transfer contact with the plate divided by L.
- p is the ℓ^p-norm p.

The kinetic and plate power fluxes, I_k and I_p, lead to the natural convection $\overline{Nu}$:

$$I_k = B\, Re^E\, \frac{\rho\, u^3}{2}\, \frac{\Pi_4}{2}\, \Pi_5 \qquad I_p = \frac{k\, \Delta T}{L}\, Nu_0\, \left\| 1-C, C\, D\, Re \right\|_p \tag{8}$$

$$\overline{Nu} = \left\| Nu_0\, [1-C]\,,\ \sqrt[2+E]{[C\, D\, Nu_0]^{3+E}\, \frac{2}{B}\, \frac{Ra}{\Xi(Pr)}}\ \right\|_p \tag{9}$$

Table 4 gives the parameters for natural convection from both external and wind-tunnel constrained plates in the three orthogonal orientations.

Table 4 derivation parameters

venue	orientation	L	Nu_0	E	B	C	D	p
external	upward	L^*	Nu_0^*	1	2	$1/\sqrt{8}$	1	1/2
internal	upward	$L'/2$	$Nu_0'/2$	1	1	1/2	1/2	1/2
external	vertical	L'	Nu_0'	1	1/2	1/2	1/4	1/2
internal	vertical	L'	Nu_0'	1	$\|1/2, 1/4\|_2$	1/2	1/4	1/2
external	downward	$L'/2$	$Nu_0'/2$	3	4	1/2	2	1
internal	downward	L'	Nu_0'	4	1/2	1/2	1	1

When the wind-tunnel is oriented with the plate surface facing upward, horizontal flow toward the plate is obstructed from two of the sides. Equation (10) gives the natural convection expected for an upward-facing plate with horizontal flow from an opposing pair of sides.

$$\overline{Nu^*} = \left\| \frac{Nu_0}{4}, \frac{{Nu_0}^{4/3}}{8} \left[\frac{Ra}{\Xi(Pr)}\right]^{1/3} \right\|_{1/2} \approx \left\| 0.341\ ,\ 0.189 \left[\frac{Ra}{\Xi(Pr)}\right]^{1/3} \right\|_{1/2} \tag{10}$$

When the plate is vertical in the wind-tunnel, horizontal flow directly toward the plate is obstructed by the wind-tunnel walls; it must flow parallel to the plate. This flow bends upward in the plane of the plate; thus parameter B is the RSS of horizontal and vertical normalized lengths:

$$\overline{Nu'} = \left\| \frac{Nu_0'}{2}\ ,\ \frac{[Nu_0'/8]^{4/3}}{\|1/4, 1/8\|_2^{1/3}} \left[\frac{Ra}{\Xi(Pr)}\right]^{1/3} \right\|_{1/2} \approx \left\| 0.682\ ,\ 0.144 \left[\frac{Ra}{\Xi(Pr)}\right]^{1/3} \right\|_{1/2} \tag{11}$$

Downward convection measured inside the wind-tunnel is not bifurcated. Apparently the fan and cowling obstruct flow from that side. The following formula is used when $V = 0$:

$$\overline{Nu} = \frac{Nu_0'}{2} + \frac{{Nu_0'}^{7/6}}{2^{5/6}} \left[\frac{Ra}{\Xi(Pr)}\right]^{1/6} \approx 0.682 + 0.806 \left[\frac{Ra}{\Xi(Pr)}\right]^{1/6} \tag{12}$$

6. Natural convection side model

The plate has 6 surfaces from which heat can flow. In order to measure natural convection from the (rough) test surface, natural convection and thermal radiation from the four sides (U_S) and back must be deducted from the total heat flow. Heat from the back surface flows through thermal insulating foam to a thin aluminum plate with a temperature sensor. This heat flow is simply $U_I\,[T_P - T_B]$, the product of the temperature difference between the plates and the thermal conductance of the foam.

The heat flow through the four sides U_S will be estimated from the plate and ambient temperatures. While the forced convective surface conductance of the sides can be modeled by integrating the local forced surface conductance, this isn't possible for natural convection generally.

The natural convection and thermal radiation for the four sides will be modeled using the fewest parameters possible. Only two parameters, L_{es} and ϵ_W, are introduced into the model. The natural convection of each side is calculated for an $L_{es} \times L_C$ area instead of its actual $L_S \times L_C$ area. The black-body radiation from each side is calculated for its actual $L_S \times L_C$ area with an effective emissivity of ϵ_W.

The flow patterns in Fujii and Imura [6] figures 14(e) and 14(f) show a plume rising from the center of an upward-facing plate fed by flow from the plate's edges. For the test surface, the upward flow of 0.467 W/K is more than twice the 0.212 W/K expected from the back and sides. Convective flow from the upward-facing test surface will draw in the air heated by the back and sides, reducing heat loss from the test surface. In order to avoid double counting the convected heat from the back and sides, they shouldn't be deducted from the plate heat (the thermal radiation is still deducted). The "reuptake" of this convected back and side heat was expected to be nearly complete; it was set to 1 to avoid introducing another degree-of-freedom into the model. Part of the error budget is devoted to the difference between actual reuptake and 1.

Not deducting side convection from upward natural convection has a benefit: the upward convection model is insensitive to L_{es}; this allows ϵ_W to be determined from upward convection alone.

The 3 mm roughness plate had its sides wrapped with duct tape, which has a different emissivity from the foam wedges forming each side surface. Some of the 1 mm roughness plate runs were with tape and some without, requiring different ϵ_W values. For taped sides $\epsilon_W \approx 0.68$; without tape $\epsilon_W \approx 0.48$.

Figure 12 shows upward convection measurements. The "clean" markers are without tape. The "3mm" markers are with tape. The trace labeled "theory" is from the upward convection formula in Jaffer [5].

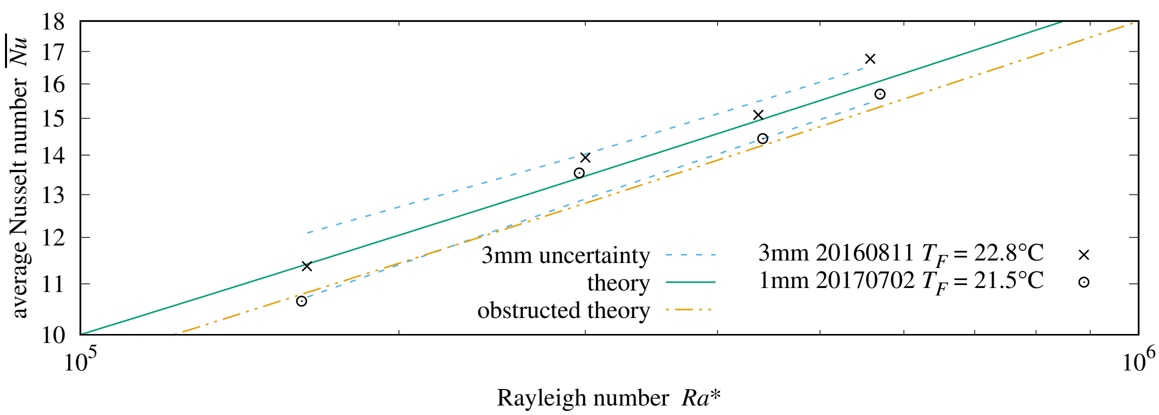

Figure 12 natural convection from upward-facing surface

In the vertical case, 1/2 of the heated air from the bottom side flows along the vertical test surface and would be double counted. And 1/2 of the air drawn by the top side comes from the vertical test surface and would be double counted. This vertical reuptake coefficient was set to 1 (of the 1/2) and allocated a portion of the error budget for the difference between the actual reuptake coefficient and 1.

With ϵ_W already determined, L_{es} was the remaining degree of freedom. Trials with vertical and downward plate measurements found that L_{es} had a value near the sum of the aluminum slab thickness 19.4 mm and the effective height of the side face of the roughness $\approx \sqrt{2}\,\varepsilon$. This is quite reasonable for a characteristic length; so it's used for L_{es}. The 3 mm roughness plate has $L_{es} \approx 23.6$ mm; 1 mm has $L_{es} \approx 21.0$ mm.

Figure 13 shows vertical natural convection measurements. Figure 14 shows measurements for downward natural convection. The traces labeled "theory" are from formulas in Jaffer [5].

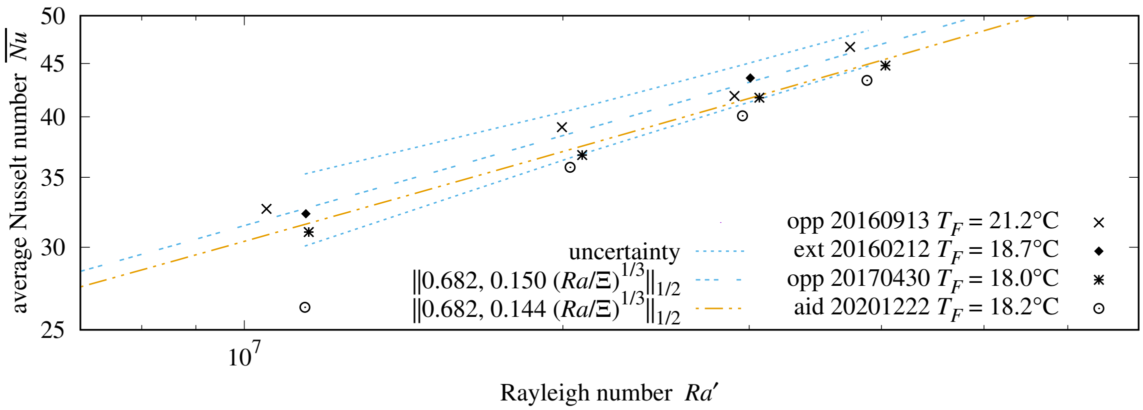

Figure 13 natural convection from vertical surface

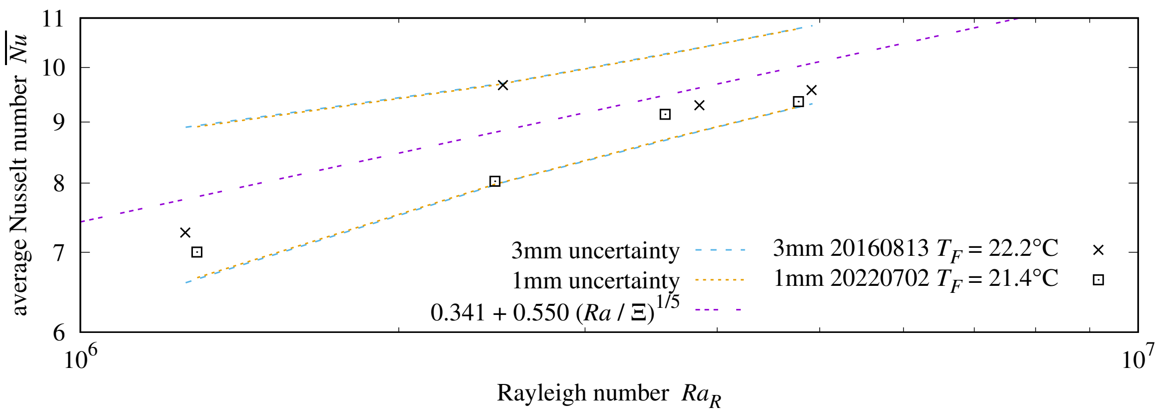

Figure 14 natural convection from downward-facing surface

Consider the (initially) vertical plate as θ decreases from 0°. As the bottom side face tilts upward, more (than half of the) heated air will rise toward the test surface. That heat will reduce the convection from the test surface. When tilted downward, the heat from the test surface will reduce the convection from the top side. To handle these cases, equation (14) includes a term $2\cos\theta\sin\theta$ whose minimum of -1 is reached at $\theta = -45°$ and a term $-2\cos\theta\sin\theta$ whose minimum of -1 is reached at $\theta = +45°$.

A side's radiative emissions compete with its convective heat transfer. Both increase with side temperature, but both act to lower that side temperature. Competitive heat transfer processes can often be modeled using the ℓ^p-norm with $p > 1$. The value of p was adjusted so that the $\Delta T = 3.8$K and $\Delta T = 11$K data points align with the theory traces in Figure 15. The optimal range is between $p = 4/3$ and $p = 3/2$; the geometric mean of those values is $p = \sqrt{2}$.

Formula (14) U_S is an amount which will be deducted from the measured heat flow. For each side, the $\ell^{\sqrt{2}}$-norm of the radiative and convective conductances is paired with the product of the convective conductance and a continuous trigonometric function of θ which goes negative when the natural convection would otherwise be double counted. Because of the triangle inequality, the $\ell^{\sqrt{2}}$-norm will be greater than the convective component; thus, each side's contribution to U_S will be positive.

No more than one reuptake process will be simultaneously active for a side. In Formula (14), the expressions $\min(0, \sin\theta, -.5\cos\theta, 2\cos\theta\sin\theta)$ and $\min(0, \sin\theta, -.5\cos\theta, -2\cos\theta\sin\theta)$ return the negative of the largest magnitude potential reuptake. Table 5 describes the natural convection parameters and function. The only effect of ϕ is to swap arguments L_F and L_W when ϕ is an odd multiple of 90°.

Table 5 natural convection parameters

$U_N(\theta, L_F, L_W, \phi)$	natural convective conductance from Jaffer [5]
θ	surface angle from vertical ($-90°$ is face up)
L_F	plate length
L_W	plate width
ϕ	rotation in plane of plate; integer multiple of $90°$
$L_C = 0.305$ m	plate length = side length
$L_S = 45.8$ mm	side thickness
$L_{es} = 19.4 \text{ mm} + \sqrt{2}\,\varepsilon$	effective side thickness for natural convection
$\epsilon_{wt} = 0.9$	wind-tunnel test chamber emissivity
$\epsilon_W \approx 0.68$ taped; 0.48 bare	effective side emissivity
h_R	black-body radiative surface conductance
$U_\epsilon = L_C\, L_S\, \epsilon_W\, \epsilon_{wt}\, h_R$	radiative emission from a side
U_S	combined sides convective and radiative deduction

U_{B0} is the test surface reuptake conductance from the back. Its $\min(0, \sin\theta)$ term is squared because the heated air from the back must flow around two right-angle edges to reach the test surface.

$$U_{B0} = -U_N(90°, L_C, L_C, 0°)\ \min(0, \sin\theta)^2 \tag{13}$$

$$\begin{aligned} U_S = {} & \|U_\epsilon, U_N(\theta - 90°, L_C, L_{es}, 0°)\|_{\sqrt{2}} \\ & + U_N(\theta - 90°, L_C, L_{es}, 0°)\ \min(0, \sin\theta, -.5\ \cos\theta, -2\ \cos\theta\ \sin\theta) \\ & + \|U_\epsilon, U_N(90° - \theta, L_C, L_{es}, 0°)\|_{\sqrt{2}} \\ & + U_N(90° - \theta, L_C, L_{es}, 0°)\ \min(0, \sin\theta, -.5\ \cos\theta, 2\ \cos\theta\ \sin\theta) \\ & + 2\ \|U_\epsilon, U_N(0°, L_{es}, L_C, \theta)\|_{\sqrt{2}} \\ & + 2\, U_N(0°, L_{es}, L_C, \theta)\ \min(0, \sin\theta) \end{aligned} \tag{14}$$

Figure 15 compares Jaffer [5] theory with measurements processed by Formulas (4, 7, 6, 13, 14):

$$\overline{h} = k \begin{cases} \max\left(\overline{Nu'}(|\cos\theta|\, Ra')/L', \overline{Nu^*}\left(|\sin\theta|\, Ra'\, [L^*/L']^3\right)/L^*\right) & \text{if } Ra' \sin\theta < -[L^*/L']^3; \\ \max\left(\overline{Nu'}(|\cos\theta|\, Ra')/L', \overline{Nu}_R\left(|\sin\theta|\, Ra'\, [L_R/L']^3\right)/L_R\right) & \text{if } Ra' \sin\theta > [L_R/L']^3; \\ \overline{Nu'}\left(|\cos\theta|\, Ra'\right)/L' & \text{otherwise.} \end{cases} \tag{15}$$

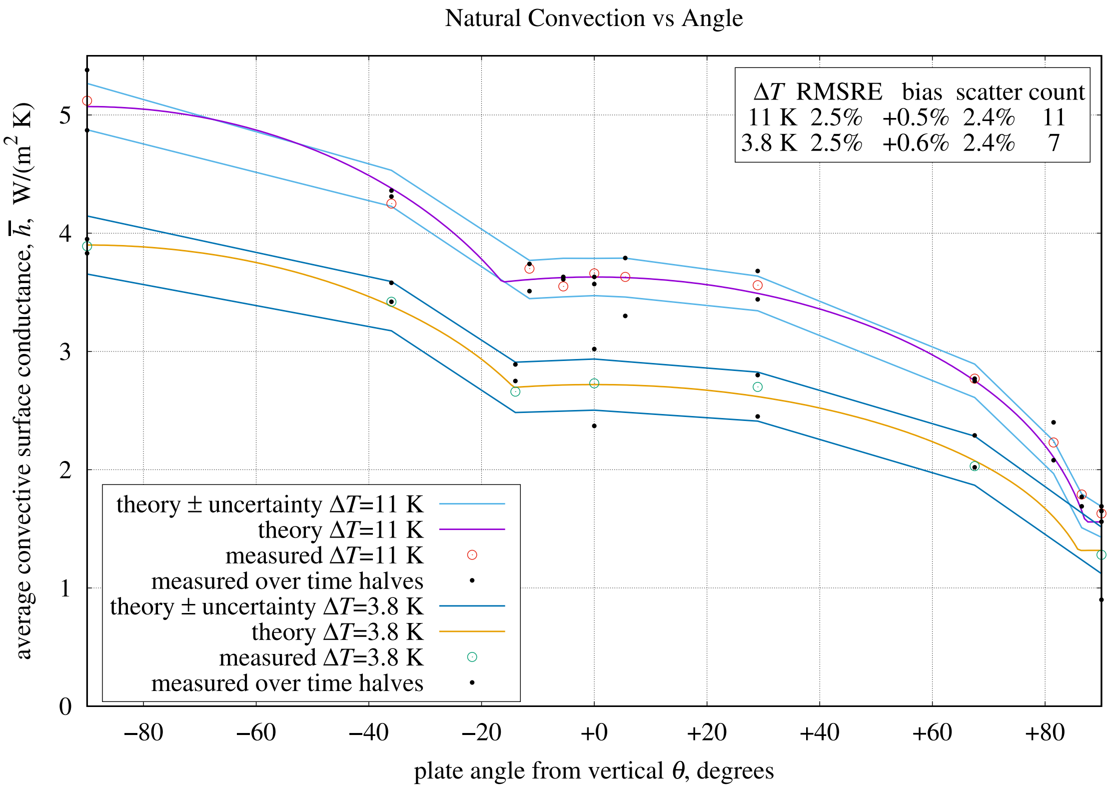

Figure 15 natural convection vs angle

7. Forced convection side model

The four sides aren't isothermal surfaces; each has a 3.5 mm metal strip exposed running the length of the side with a wedge of extruded polystyrene foam (XPS) insulation filling the 27 mm 45° chamfer. Each point's effective surface conductance will depend on the temperature profile along the side.

A point on the side which is near to metal will have a large conductance. Summing the conductivity divided by the shortest distance to metal at each angle will be roughly proportional to the local conductance (see Figure 9). The conductance through a slab with parallel isothermal faces is $k\,A/d$. The ratio of the slab conductance to the slab sum is 0.637, which is used to normalize the calculated conductivities.

In forced air the four sides have three distinct behaviors. The forced air flows parallel to the long dimension on two sides but flows into the windward side and away from the leeward side. The windward and leeward sides don't contribute forced convection.

The smooth turbulent forced convective component for the two parallel sides $U_{fl}(u)$ is computed by averaging the local forced convective surface conductance in series with the insulation thermal conductance over the area of the sides. Laminar flow isn't modeled; the lower bound of integration is $Re_0 = 450$. The expected convection through the two parallel sides is 9% of the convection from the 3 mm rough surface at 4 m/s airspeed.

8. **Mixed convection side model**

Each $\ell^{\sqrt{2}}$-norm instance of a call to U_N is replaced by a call to U_M, with first argument $U_{fl}(u)$ or $U_{fi}(u)$. The reuptake instances of $U_N(\theta, L_F, L_W, \phi)$ are changed to the equivalent $U_M(0, \theta, L_F, L_W, \phi, 0°)$.

Table 6 mixed conductance functions and parameters

$U_{fl}(u)$	level flow side forced thermal conductance
u	bulk flow velocity
$U_{fi}(u) = 0$	tilted flow side forced thermal conductance
$U_M(U_F, \theta, L_F, L_W, \phi, \psi)$	mixed convective conductance from Jaffer [2]
U_F	forced thermal conductance
θ	surface angle from vertical ($-90°$ is face up)
L_F	forced characteristic length
L_W	other plate dimension
ϕ	rotation in plane of plate; integer multiple of $90°$
ψ	angle of fluid flow from vertical ($0°$ is upward)

$$\begin{aligned}
U_S(u) = {} & \|U_\epsilon, U_M(U_{fl}(u), \theta - 90°, L_C, L_{es}, 0°, \psi)\|_{\sqrt{2}} \\
& + U_M(0, \theta - 90°, L_C, L_{es}, 0°, 0°)\ \min(0, \sin\theta, -.5\ \cos\theta, -2\ \cos\theta\ \sin\theta) \\
& + \|U_\epsilon, U_M(U_{fl}(u), 90° - \theta, L_C, L_{es}, 0°, \psi)\|_{\sqrt{2}} \\
& + U_M(0, 90° - \theta, L_C, L_{es}, 0°, 0°)\ \min(0, \sin\theta, -.5\ \cos\theta, 2\ \cos\theta\ \sin\theta) \\
& + 2\ \|U_\epsilon, U_M(U_{fi}(u), 0°, L_{es}, L_C, \theta, \psi)\|_{\sqrt{2}} \\
& + 2\, U_M(0, 0°, L_{es}, L_C, \theta, 0°)\ \min(0, \sin\theta)
\end{aligned} \tag{16}$$

Equation (16) is for horizontal flow ($\psi = 90°$). For inclined flow, swap the values of U_{fl} and U_{fi}. When u is large, $U_S(u)$ approaches the sum of the forced convection conductances. When $u = 0$, $U_S(0) = U_S$ of Formula (14).

9. Measurement Uncertainties

Following Abernethy, Benedict, and Dowdell [7], the final steps in processing an experiment's data are:

1) Using equation (6), calculate the sensitivities of convected power $\overline{h}\,A\,\Delta T$ per each parameter's average over the measurement time-interval;
2) multiply each sensitivity by its estimated parameter bias to yield the component uncertainties;
3) calculate combined bias uncertainty as the root-sum-squared (RSS) of the component uncertainties;
4) calculate the RSS combined measurement uncertainty as the RSS of the combined bias uncertainty and twice the product of the rotation rate sensitivity and variability.

Table 7 Estimated measurement uncertainties, bi-level 3mm roughness at $Re = 59593$.

Symbol	Nominal	Sensitivity	Bias	Uncertainty	Component
ΔT	9.47K	+12.2%/K	0.10K	1.22%	LM35C differential
P	101kPa	+0.0009%/Pa	1.5kPa	1.28%	MPXH6115A6U air pressure
C_{pt}	4.69kJ/K	+0.024%/(J/K)	47J/K	1.14%	plate thermal capacity
η	0.401	+180%	0.014	2.52%	anemometer calibration
ς	6.00mm	+11299%/m	100um	1.13%	post height
				3.50%	combined bias uncertainty
Symbol	**Nominal**	**Sensitivity**	**Variability**	**Uncertainty**	**Component**
ω	905r/min	+0.081%/(r/min)	5.2r/min	0.43%	fan rotation rate
				3.60%	RSS combined uncertainty

Table 8 Estimated measurement uncertainties, bi-level 1mm roughness at $Re = 55935$.

Symbol	Nominal	Sensitivity	Bias	Uncertainty	Component
ΔT	10.2K	+11.8%/K	0.10K	1.18%	LM35C differential
P	100.0kPa	+0.0008%/Pa	1.5kPa	1.26%	MPXH6115A6U air pressure
C_{pt}	4.24kJ/K	+0.028%/(J/K)	42J/K	1.18%	plate thermal capacity
η	0.340	+195%	0.003	0.66%	anemometer calibration
u_u	6.381	+2.44%	0.100	0.24%	diffuser airflow upper bound
L_T	8.34mm	+9361%/m	100um	0.94%	post length
L_m	3.57mm	+473%/m	500um	0.24%	side metal strip width
ϵ_{rs}	0.040	+21.3%	0.010	0.21%	test-surface emissivity
ϵ_{wt}	0.900	+9.46%	0.025	0.24%	wind-tunnel emissivity
				2.46%	combined bias uncertainty
Symbol	**Nominal**	**Sensitivity**	**Variability**	**Uncertainty**	**Component**
ω	1.03kr/min	+0.065%/(r/min)	2.5r/min	0.16%	fan rotation rate
				2.48%	RSS combined uncertainty

Tables 7 and 8 list the sensitivity, bias, and uncertainty for each component contributing more than 0.2% uncertainty for the 3 mm and 1 mm roughness plates, respectively.

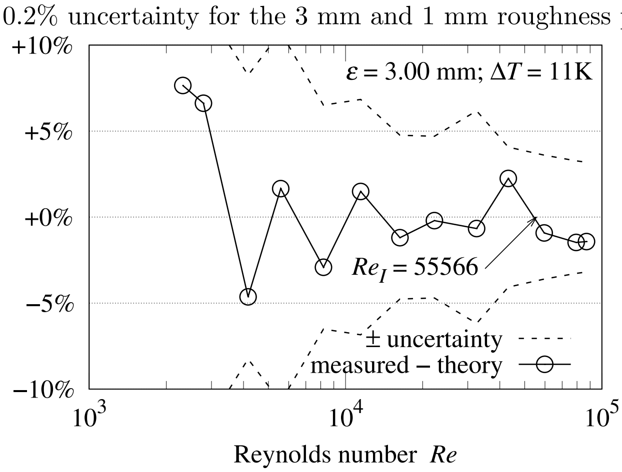

Figure 16 convection versus theory 3 mm

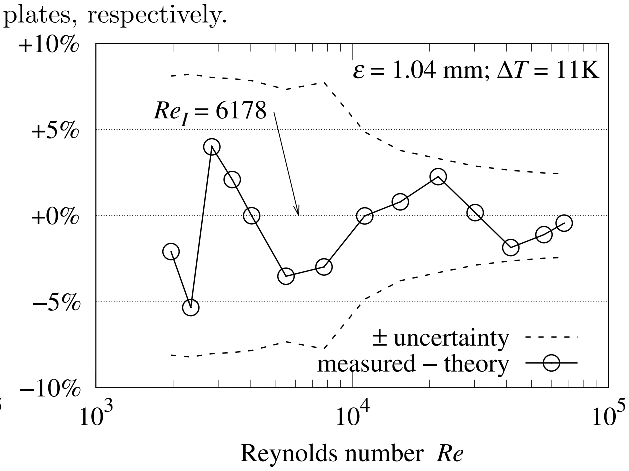

Figure 17 convection versus theory 1 mm

10. **Conclusion**

The Convection Machine was employed to collect data about forced, natural, and mixed convection, capturing 110 data-sets with the 3 mm roughness plate and 380 with the 1 mm roughness plate. Each run had a duration of 102 minutes, totaling 880 hours over two and a half years.

The measurements obtained were the basis for two papers: *Skin-Friction and Forced Convection from Rough and Smooth Plates* [1] and *Mixed Convection From an Isothermal Rough Plate* [2]. Graphs of the data from the two papers are available at: `http://people.csail.mit.edu/jaffer/convect`

Acknowledgments

Thanks to John Cox (1957-2022) and Doug Ruuska for machining the bi-level plates. Thanks to Martin Jaffer and Roberta Jaffer for their assistance and problem-solving suggestions.

11. **References**

[1] Aubrey Jaffer. Skin-friction and forced convection from rough and smooth plates. *Thermo*, 3(4):711–775, 2023, doi:10.3390/thermo3040040.

[2] Aubrey G. Jaffer and Martin S. Jaffer. Mixed convection from an isothermal rough plate, 2024.

[3] Hermann Schlichting. *Boundary-Layer Theory*. McGraw Hill, New Delhi, seventh edition, 2014. Translated by Kestin, J.

[4] R.W. Rice. Emittance factors for infrared thermometers used for wood products. *Wood and Fiber Science*, 36:520–526, 2004.

[5] Aubrey Jaffer. Natural convection heat transfer from an isothermal plate. *Thermo*, 3(1):148–175, 2023, doi:10.3390/thermo3010010.

[6] Tetsu Fujii and Hideaki Imura. Natural-convection heat transfer from a plate with arbitrary inclination. *International Journal of Heat and Mass Transfer*, 15(4):755–764, 1972, doi:10.1016/0017-9310(72)90118-4.

[7] R.B. Abernethy, R.P. Benedict, and R.B. Dowdell. Asme measurement uncertainty. *ASME. J. Fluids Eng.*, 107(2):161–164, 1985, doi:10.1115/1.3242450.

12. Appendix: rough to smooth turbulence transition

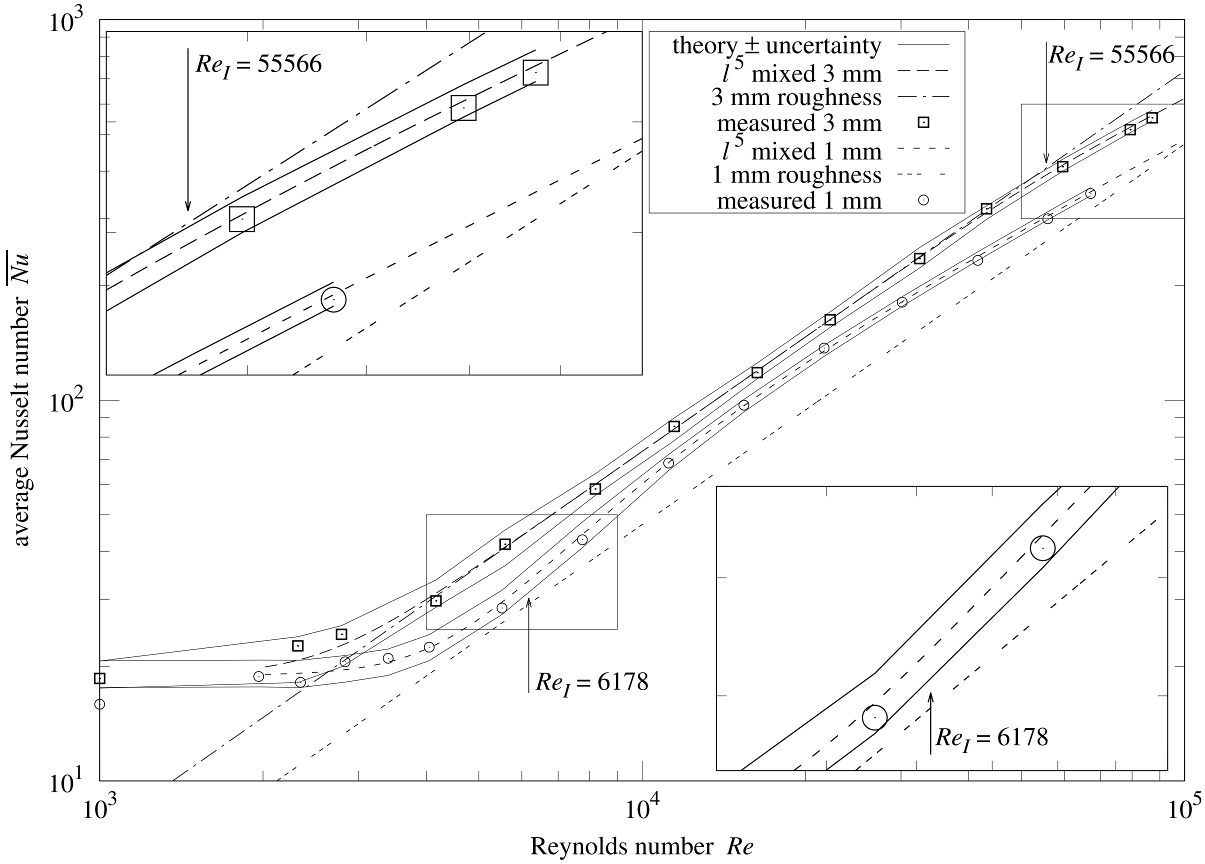

Figure 18 convection and measurement uncertainties from rough plates